Beneficial Effects of Microwave-Assisted Heating *versus* Conventional Heating in Noble Metal Nanoparticle Synthesis

Naween Dahal,[†] Stephany García,[†] Jiping Zhou,[‡] and Simon M. Humphrey[†,*]

[†]Department of Chemistry and Biochemistry, The University of Texas at Austin, 1 University Station A5300, Austin, Texas 78712-0165, United States and [‡]Center for Nano- and Molecular Science, The University of Texas at Austin, 1 University Station C2201, Austin, Texas 78712, United States

ABSTRACT An extensive comparative study of the effects of microwave *versus* conventional heating on the nucleation and growth of near-monodisperse Rh, Pd, and Pt nanoparticles has revealed distinct and preferential effects of the microwave heating method. A one-pot synthetic method has been investigated, which combines nucleation and growth in a single reaction *via* precise control over the precursor addition rate. Using this method, microwave-assisted heating enables the convenient preparation of polymer-capped nanoparticles with improved monodispersity, morphological control, and higher crystallinity, compared with samples heated conventionally under otherwise identical conditions. Extensive studies of Rh nanoparticle formation reveal fundamental differences during the nucleation phase that is directly dependent on the heating method; microwave irradiation was found to provide more uniform seeds for the subsequent growth of larger nanostructures of desired size and surface structure. Nanoparticle growth kinetics are also markedly different under microwave heating. While conventional heating generally yields particles with mixed morphologies, microwave synthesis consistently provides a majority of tetrahedral particles at intermediate sizes (5−7 nm) or larger cubes (8+ nm) upon further growth. High-resolution transmission electron microscopy indicates that Rh seeds and larger nanoparticles obtained from microwave-assisted synthesis are more highly crystalline and faceted *versus* their conventionally prepared counterparts. Microwave-prepared Rh nanoparticles also show approximately twice the catalytic activity of similar-sized conventionally prepared particles, as demonstrated in the vapor-phase hydrogenation of cyclohexene. Ligand exchange reactions to replace polymer capping agents with molecular stabilizing agents are also easily facilitated under microwave heating, due to the excitation of polar organic moieties; the ligand exchange proceeds with excellent retention of nanoparticle size and structure.

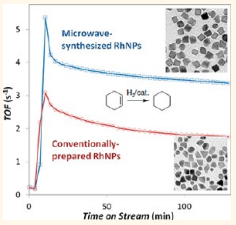

KEYWORDS: rhodium nanoparticles · palladium nanoparticles · platinum nanoparticles · microwave synthesis · polyol method · seeding and growth · ligand exchange · shape control

The morphology of metal nanoparticles directly influences their catalytic selectivity due to the intrinsic relationship between surface structure and reactivity.[1−4] This important correlation has been explored extensively for a multitude of single-crystal surfaces of various catalytically important metals, particularly for the noble metals.[5−7] For example, simple olefin hydrogenation reactions proceed with high selectivity to give distinct but different products in direct response to the structure of the exposed noble metal surface.[8,9] Noble metal nanoparticle catalysts are therefore of immense current interest in heterogeneous catalysis because they offer far superior surface areas in comparison to single crystals.[10] Traditionally, noble metal single crystals have been mechanically modified to expose exclusively certain Miller faces in order to impart desired catalytic selectivity. Nanoparticle analogues cannot be easily prepared by mechanical methods because physical grinding of bulk crystalline metal provides only poorly defined nanosized fragments with mixed surface structures.[11,12] Instead, well-defined nanoparticles are most conveniently prepared *via* solution-based, "bottom-up" methods. Most commonly, molecular precursors are reduced in the presence of surface passivation agents, which prevent aggregation and may also impart some control in the growth process. Solution-phase nanoparticle synthesis has thus attracted significant recent attention as a means to prepare near-monodisperse nanoparticles with particular predominant surface structures. Success in this regard requires fine control over both the nucleation and subsequent growth of the nanoparticles in solution, which is not trivial. Nucleation of small nanoparticle clusters in the solution phase is instigated by supersaturation of the molecular precursor, akin to regular crystallization kinetics.[13−16] The kinetic parameters of this step are somewhat difficult to control since supersaturation-induced nucleation events are very fast. Uncontrolled and non-uniform nucleation commonly gives rise to a distribution of "seed" nucleates of a range of sizes and morphologies. This commonly leads to the growth of larger, but similarly non-uniform, nanostructures. Solvent,

* Address correspondence to smh@cm.utexas.edu.

Received for review April 25, 2012 and accepted October 3, 2012.

Published online October 03, 2012
10.1021/nn3038918

© 2012 American Chemical Society

temperature, and identity of the metal precursor offer limited control over the nucleation process. However, overgrowth of seed particles is governed by much slower kinetics. Therefore, manipulation of growth kinetics has been widely reported as the most convenient means to control final nanoparticle morphology. Selective addition at certain (higher energy) faces of the seed particles has been demonstrated to provide reasonable shape control,[17,18] while the promotion of digestion or ripening processes can also improve nanoparticle uniformity.[19,20] Specific to the case of noble metals that exhibit a face-centered cubic (fcc) lattice structure, control of growth kinetics has been shown to yield selectively a majority of cubes,[16,21] tetrahedra,[22−25] tetrapods,[26,27] or lower symmetry nanoparticles.[28]

New methods by which to prepare noble metal nanoparticles (NPs) with well-defined surface structure have attracted significant interest over the past few years[26,29−46] due to the importance of metals such as Rh, Pd, and Pt as heterogeneous catalysts in a range of critical industrial processes (*e.g.*, regioselective hydrogenation, benzene reduction, NO_x reduction). Specifically for Rh, previous studies have identified suitable conditions for the preparation of a range of RhNP morphologies *via in situ* reduction of Rh(III) precursors in hot, reducing solvents (commonly high boiling-point polyols).[26,29,30,47] Most recently, these basic synthetic strategies have been refined to significantly improve morphological control by paying particular attention to the kinetics of NP nucleation and growth. Notable examples include the correlation between polyol oxidizing strength and resulting RhNP structure[30] and the direct manipulation of growth kinetics as a function of molecular Rh precursor addition rate.[45] As a result of this work, it is now possible to prepare RhNPs with particular surface structures to a high degree of specificity. It is therefore somewhat striking that little or no attention has yet been paid to the effects of the heating method upon RhNP synthesis. Previous studies have relied on conventional (convective) heating of solvents, which involves slow heating and cooling of the solvent medium and the potential for non-uniform temperatures. Microwave-assisted heating has attracted significant interest in a range of synthetic fields, including organic synthesis[48,49] and inorganic materials preparation,[50,51] owing to the fast reaction times, high-throughput capabilities, and beneficial crystallization effects induced by unusual, localized "hotspot" heating.[50] Specifically regarding metal NP synthesis, microwave chemistry has been employed recently in the synthesis of semiconductor NPs,[52,53] f-block oxide nanostructures,[54] and some interesting heterobimetallic d-metal NP catalysts.[55−57] However, a systematic and comparative study of the effects of microwave irradiation upon homometallic noble metal NP nucleation and growth still does not exist.

The results from this study reveal the comparative effects of microwave heating (MwH) *versus* conventional heating (CvH) in RhNP synthesis. The popular polyol reduction method has been coupled to syringe pump control of precursor addition rate to achieve a convenient and highly reproducible procedure. This method is also shown to be more broadly applicable, as demonstrated in the synthesis of Pd and PtNPs, with comparable control over size and structure. In-depth quantitative studies indicate a number of beneficial effects of the MwH method: (a) under otherwise identical reaction conditions, NP morphological control and crystallinity are significantly improved due to MwH; (b) the Mw-induced nucleation process is faster and more reproducible compared to CvH methods; and (c) Mw synthesis results in cubic RhNPs that are more highly active hydrogenation catalysts, which do not require high-temperature pretreatment and thus retain their morphology. In addition, it is shown that MwH greatly enhances the ability to substitute polymer capping agents with monomeric capping agents, which is kinetically disfavored using CvH.

RESULTS AND DISCUSSION

Optimized Seeding and Growth Method. Previous studies[26,45] of RhNP synthesis under CvH heating have shown that syringe pump control of precursor addition rate may lead to improved experimental reproducibility in comparison to reactions where a set amount of precursor is simply refluxed for a given period of time. Moreover, adjustment of the addition rate during the experiment can offer some degree of control of the kinetics of particle growth, which can in turn lead to varying degrees of morphological control.[45] In our work, all RhNP syntheses were performed using a highly reproducible and convenient one-pot method, which has been identified and optimized, through a large number of experiments performed in ethylene glycol at 150 °C. The multistep method combines nucleation and growth without the need to isolate and purify intermediates. Reactions were conveniently executed using a programmable syringe pump that ensured high experimental reproducibility. In this comparative study of NP formation, it is important to note that precisely the same method and apparatus have been used in all reactions except for the heating method. The glassware assembly used was designed to fit directly inside a large MwH reactor cavity (Scheme S1 in Supporting Information). In all instances, the precursor addition profile as shown in Scheme 1 was followed. An initial aliquot of $RhCl_3$ (20 mg, 0.1 mmol) was rapidly injected into hot ethylene glycol in the presence of an excess of poly(vinylpyrrolidone) (PVP); this affected immediate nucleation (Scheme 1A) of small isotropic Rh seeds. A subsequent period of isothermal stirring promoted size focusing of the seeds (Scheme 1B). Controlled growth was then achieved by much slower addition of a second aliquot of $RhCl_3$, such that the low concentration of monomer in solution favored only overgrowth of existing seeds and disfavored nucleation of new particles (Scheme 1C). In accordance with this supposition, the

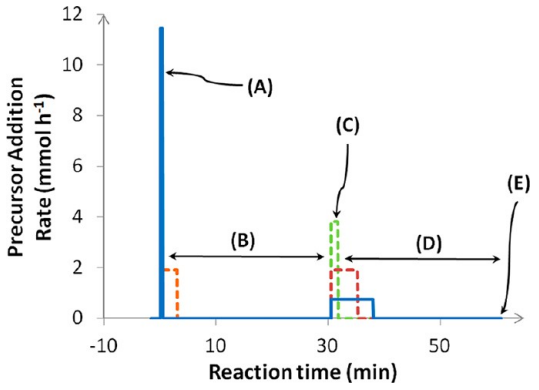

Scheme 1. Syringe pump precursor addition rate programs employed to achieve controlled nucleation and growth: optimized conditions (blue) and examples of alternatives also studied (dashed lines); (A) nucleation phase; (B) seed ripening; (C) nanoparticle overgrowth; (D) nanoparticle ripening; (E) reaction quenched at 0 °C.

total amount of precursor added in the growth phase was found to correlate directly with the resulting mean RhNP size. A further period of isothermal ripening and rapid cooling was used to obtain the final RhNP products (Scheme 1D,E).

RhNP Seeds. First, for reactions performed under both CvH and MwH at 150 °C, seed particles that were formed immediately after precursor addition in the rapid nucleation phase were analyzed using transmission electron microscopy (TEM; Figures 1 and 2). The effect of precursor addition rate was also studied for total addition periods of 0.25−3 min in which the total amount of added precursor remained constant. The data are summarized in Figure 3A and reveal a number of clear and consistent trends. First and foremost, the average RhNP seed size obtained under MwH was consistently 1−1.5 nm larger than that obtained at the same temperature under CvH, irrespective of precursor addition rate (Figure 3A, open symbols). This is indicative of significant differences in the nucleation processes under the two types of heating. The larger seeds that were generated by MwH presumably formed due to faster and more efficient nucleation, followed by immediate overgrowth by further precursor. Broad adjustment of the precursor addition rate (3.8−45.8 mmol h^{-1}) indicated that above a lower limit of 3.8 mmol h^{-1} (20 cm^3 h^{-1}) there was no noticeable effect of increased addition rate on the resulting particle size. This was presumably because supersaturation-induced nucleation had been achieved in all cases. TEM analysis of RhNP seeds (Figures 1 and 2) revealed that the MwH-prepared samples consisted of cuboctahedra and icosahedra. Meanwhile, the smaller CvH-prepared seeds were initially highly anisotropic, with multiple and irregular corners and appendages. These observations strongly suggest that Mw irradiation is effective for the instantaneous access of thermodynamically favored products. Meanwhile, CvH at the same temperature tended to yield initially a majority of kinetically favored structures, presumably due to less effective energy transfer into the solution. Below the established minimal precursor addition limit, much larger RhNPs were observed under both heating methods (Figure 3A).

All RhNP seeds were analyzed similarly after the 30 min ripening period, during which time reactions were stirred at 150 °C without addition of further precursor (Figure 3A, closed symbols). Ripening was observed in all cases and for both heating methods, with approximately 1 nm increase in mean particle sizes (Figures S1 and S2). The increase in particle size was found to be very constant for Mw-assisted reactions but somewhat erratic for CvH. The initial structural anisotropy in the CvH-prepared seeds was partially reduced after the ripening phase, presumably *via* dissolution and redistribution of the most high-energy facets.[13] Longer ripening times did not result in significant changes to the seed compositions. High-resolution TEM (HRTEM) microscopy was performed on MwH-RhNP seeds formed 30 s after addition of 0.1 mmol of $RhCl_3$ precursor (Figure S1A) and on the same seeds after continuous heating for 30 min (Figure S1B). Interestingly, after only 30 s of Mw irradiation, the majority of particles appeared to be already crystalline without clear evidence of polycrystallinity.

To further probe the effect of Mw-induced nucleation, premixed solutions of $RhCl_3$ and PVP polymer in ethylene glycol were stirred at 76 °C under MwH (determined to be just below the nucleation temperature of $RhCl_3$). Then, a high power pulse of MwH was applied to rapidly bring the internal temperature to 150 °C in only 55 s. At this point, the reduced solutions were immediately quenched in an ice−water bath. Analysis of the products by TEM revealed in all cases very small RhNPs with a range of morphologies (2.4 ± 0.9 nm obtained from 0.1 mmol $RhCl_3$; Figure S2A); it is interesting that the particles obtained were all significantly smaller than those obtained using the optimized method coupled to syringe pump delivery of the precursor after 30 s of heating (4.1 ± 1.1 nm). Evidently, while MwH is more efficient than CvH at promoting uniform nucleation under identical conditions, control of precursor concentration during the growth phase is also very important. Furthermore, when the small RhNPs obtained from the instantaneous MwH method were continuously heated for 30 min, a significant degree of ripening was observed to provide 4.5 ± 0.9 nm Rh cuboctahedra. However, while these RhNPs are similar in size to the particles obtained using the syringe pump method, they were significantly less morphologically well-defined (Figure S2A). In support of these observations, HRTEM analysis of the small MwH-RhNPs obtained from the 55 s pulsed experiment (Figure S2B) revealed anisotropic structures with only localized regions of ordered fcc Rh lattice structures, supported by lack of coherent diffraction in the fast

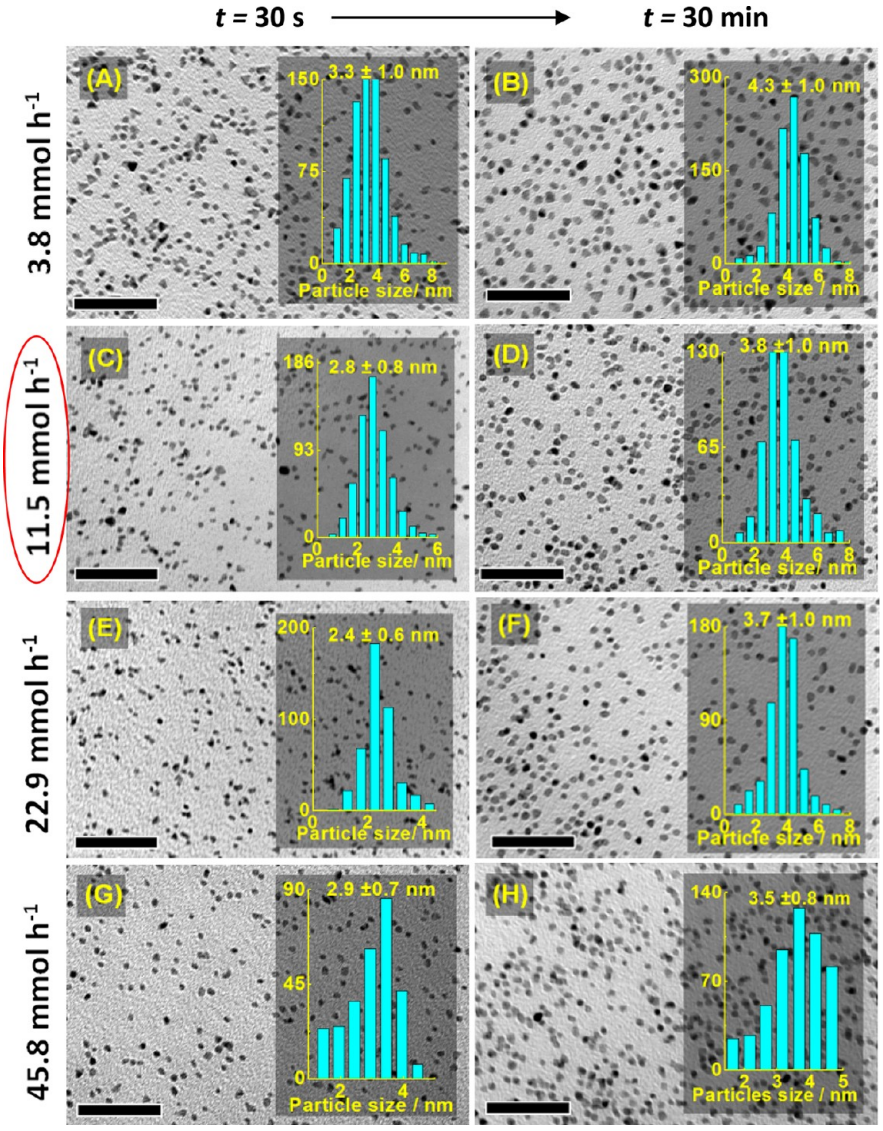

Figure 1. TEM images of CvH-RhNP seeds before and after ripening and as a function of precursor addition rate; the optimal seeds are shown in (D); scale bars = 50 nm.

Fourier transform (FFT) map of the bulk sample. In direct contrast, the same particles poststirring for 30 min were generally very well-defined, single-crystalline structures that exhibited {111}, {200}, and {220} lattice fringes throughout the sample (Figure S3A,B).

Controlled RhNP Growth. Controlled growth of the RhNP seeds was achieved by slow injection of further molecular precursor after the ripening phase. In all experiments, CvH and MwH seeds obtained from 11.5 mmol h^{-1} nucleation reactions were employed because these were consistently the most monodisperse particles (Figures 1D and 2D). The results of this experiment gave the clearest evidence for the beneficial effects of Mw irradiation in terms of both morphological control and particle crystallinity. The overall comparative trends in growth are summarized in Figure 3B. Excellent control of nanoparticle size as a function of total added precursor was achieved under both modes of heating. It was apparent from averaged data obtained from a number of experiments in which the precursor concentration was maintained significantly below the limit required for nucleation that an optimized addition rate of 0.75 mmol h^{-1} consistently favored exclusive overgrowth of the existing seeds. Controlled overgrowth under both forms of heating is also evidenced by the fact that the smaller CvH-prepared seeds resulted in accordingly smaller particles (Figure 3B, blue data) as compared with those obtained for the larger MwH-derived seeds (Figure 3B, red data). However, closer inspection of growth products obtained from the two heating methods revealed distinct differences in terms of predominant particle morphologies. As has been observed previously by others,[30,45−47] RhNP growth under CvH was dominated by isotropic, layer-by-layer growth (Figure 4). Initial batches of seeds that exhibited mixed morphologies were grown into

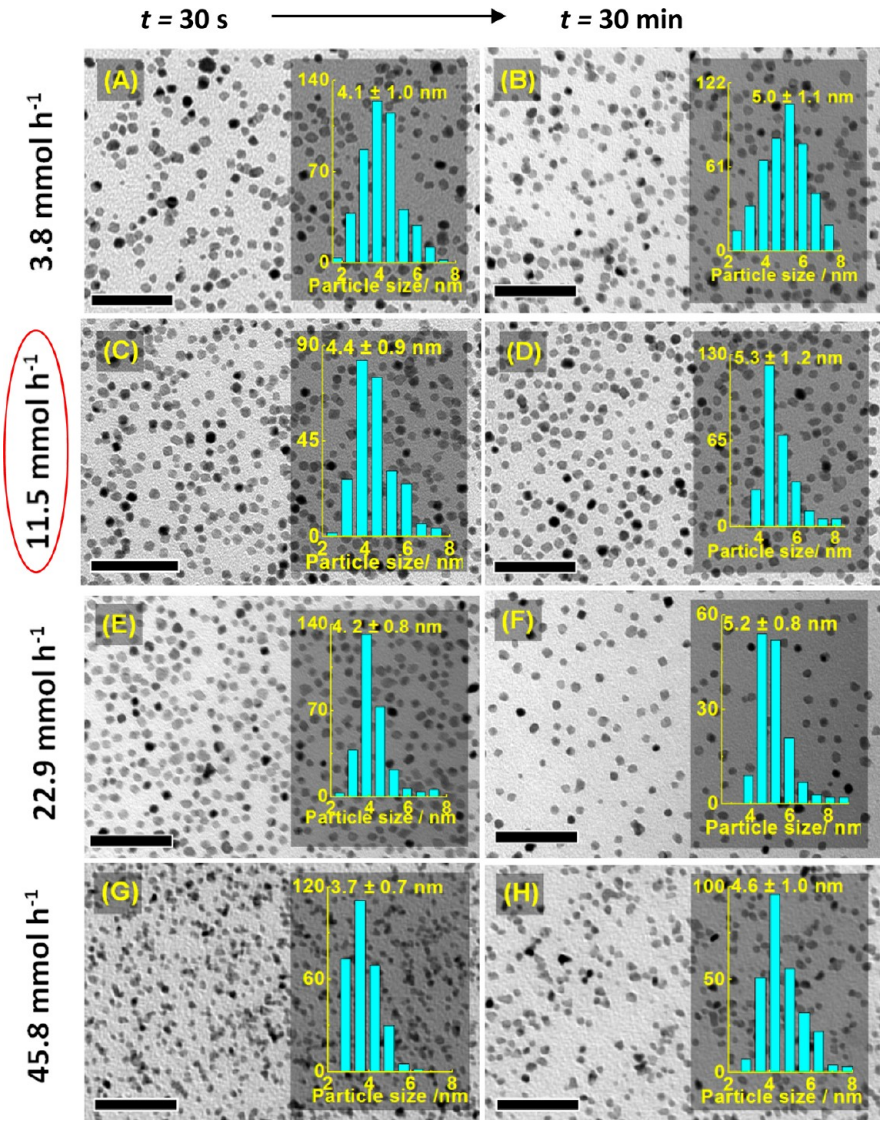

Figure 2. TEM images of MwH-RhNP seeds before and after ripening and as a function of precursor addition rate; the optimal seeds are shown in (D); scale bars = 50 nm.

incrementally larger particles with an approximately equal distribution of morphologies. The observed transfer of morphology from Rh seeds to larger NPs by a simple, templated route was most likely observed because CvH at 150 °C was not sufficient to force the reorganization of individual particles into thermodynamically more favored structures. It should also be noted that PVP utilized as the sole stabilizing agent in this study is generally accepted to offer very limited structure-directing properties.[26,30,45−47] A statistical analysis of proportional particle morphology *versus* mean RhNP size (Figure 4H) shows that no particular morphology was dominant at any size.

These findings are in contrast to what was observed for RhNP growth under Mw irradiation (Figure 5): a much clearer morphological pattern was observed, in which the highly isotropic seeds (*vide supra*) underwent growth *via* slow precursor addition to yield consistently a majority of faceted particles at intermediate sizes (5−8 nm). These consisted of mainly tetrahedral or rhombic structures (45−60% occurrence). Such a growth pattern would suggest preferential precursor addition to {100} faces of the seeds, thus resulting in more {111} exposed faces.[15−17] Strangely, however, upon further growth, the RhNPs consistently favored evolution toward cubic structures that were always found to be the dominant morphology (>70%) for Mw-prepared RhNPs above 10 nm (Figure 5G,H). The observed terminal conversion of tetrahedra to cubes suggests a reversal of preferential growth onto {111} faces to give eventual {100} cubic faces. In comparison to some pertinent previous studies by the groups of Schaak, Tilley, and Xia, anisotropic morphologies are usually favored under kinetically controlled conditions.[26,30,36,45−47] Since Mw heating is very rapid and is effective in energy transfer into solutions of polar solvents, it presumably favors monomer addition and reorganization to the highest energy sites (*e.g.*, corners

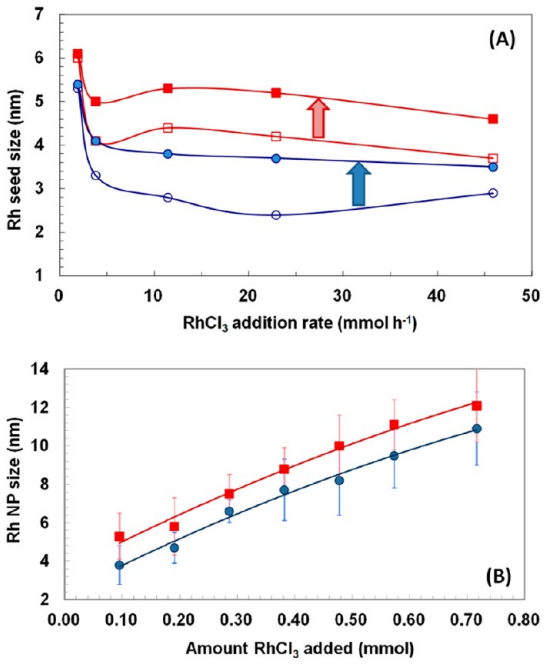

Figure 3. (A) Average sizes of initial Rh seeds (open symbols) and after ripening (solid symbols) as a function of precursor injection rate. (B) Size and standard deviation of RhNP growth products as a function of the amount of added precursor; conventional = blue; microwave = red.

and edges). Thus, epitaxial growth mechanisms are disfavored. In contrast, CvH is less effective or selective and favors greater morphological diversity in RhNP synthesis.

A series of additional experiments were conducted to examine the effect of temperature and faster precursor addition in the growth phase for both MwH and CvH reactions. These data are summarized in Figures S4−S7 and clearly show that both lower reaction temperatures and higher precursor injection rates during the growth phase favored highly anisotropic growth to yield a majority of tetrahedral structures, as has been observed previously by others.[24,33,36] Meanwhile, reactions conducted at significantly higher temperature (190 °C) gave poorly defined products in all instances.

X-ray powder diffraction analysis (XRPD) of dry samples of the RhNPs from the two heating methods confirmed bulk crystallinity corresponding closely to fcc Rh metal; the broadened reflections are indicative of small nanostructures (Figure 6). Samples of identical masses were exposed at a fixed scan rate, and in all cases, the total diffraction intensity was approximately double for the Mw-prepared samples. This is most likely because RhNPs from the MwH route were more highly crystalline in nature (*i.e.*, less twinned than the CvH-NPs). In addition, microanalysis studies by combustion and ICP-OES studies of RhNPs performed on samples from both heating methods suggested incorporation of similar amounts of PVP polymer in both cases (Table S1), so the amounts of Rh in each sample were therefore also similar. The trends in ratios of integrated peak areas for the (111) and (200) reflections (Table 1) are in agreement with the proportional morphology data (Figures 4H and 5H), assuming that the measured X-ray intensity for each reflection is proportional to the coherence length of a crystal of a given morphology. It has been previously observed for RhNPs that 12.7 nm cubes with six {100} facets exhibited $I_{(111)}/I_{(200)} = 1.8$;[36] 4.9 nm Rh cuboctahedra with six {100} and eight {111} facets gave $I_{(111)}/I_{(200)} = 3.1$;[26] hexagonal and triangular plate RhNPs with mostly {111} facets showed significantly higher intensity ratios of $I_{(111)}/I_{(200)} = 3.6-12.5$.[58] The experimentally determined $I_{(111)}/I_{(200)}$ ratios of all particles obtained in this study all lie in the range of 2.21−2.97. The smallest RhNPs from CvH that were found to be most anisotropic gave the lowest intensity ratio, indicating a dominance of {100} facets. Upon growth, the intensity ratios of Cv-prepared RhNPs increased in line with the appearance of a larger diversity of shapes, with $I_{(111)}/I_{(200)}$ ratios similar to that previously observed for cuboctahedral/icosahedral RhNPs. The intensity ratio was also found to decrease significantly for the largest MwH-RhNPs as would be predicted for an increased proportion of cubes that were experimentally observed by TEM.

HRTEM characterization was employed to probe any subtle structural differences in similar-sized nanoparticles obtained by the two heating methods. Particles from a number of separate experiments were studied, and a representative set is presented in Figure 7 (see Figures S8 and S9 for further images). The CvH-RhNPs were consistently found to be anisotropic, with morphologies intermediate between spheres and tetrahedra/square plates (Figures 7A and S8). Lattice fringes were not readily apparent in the CvH-RhNPs, although crystallization was observed *in situ* under the electron beam, after which only {111} lattice fringes were observed (Figure 7B). Since the bulk XRPD of the same samples (Figure 6) showed diffraction from a number of low Miller index faces, it seems that the CvH-RhNPs may be largely twinned in the as-synthesized form and underwent further ordering in the electron beam. The wide-area FFT from approximately 25 individual particles does not show evidence of additional lattice fringes (Figure 7C).[45] In contrast, the MwH-RhNPs were generally spherical in shape and appeared to be already highly crystalline, displaying well-ordered lattice fringes throughout the sample (Figures 7D and S9). This observation may again be due to the relative amounts of PVP incorporated into the samples based on the particular method. Figure 7E shows two overlapping particles, displaying between them three distinct *d* spacings of 0.21 nm (111), 0.19 nm (200), and 0.13 nm (220). The corresponding wide-area FFT of a number of MwH-RhNPs (Figure 7F) seems to indicate that the particles are mostly icosahedral with a majority of {111} fringes in

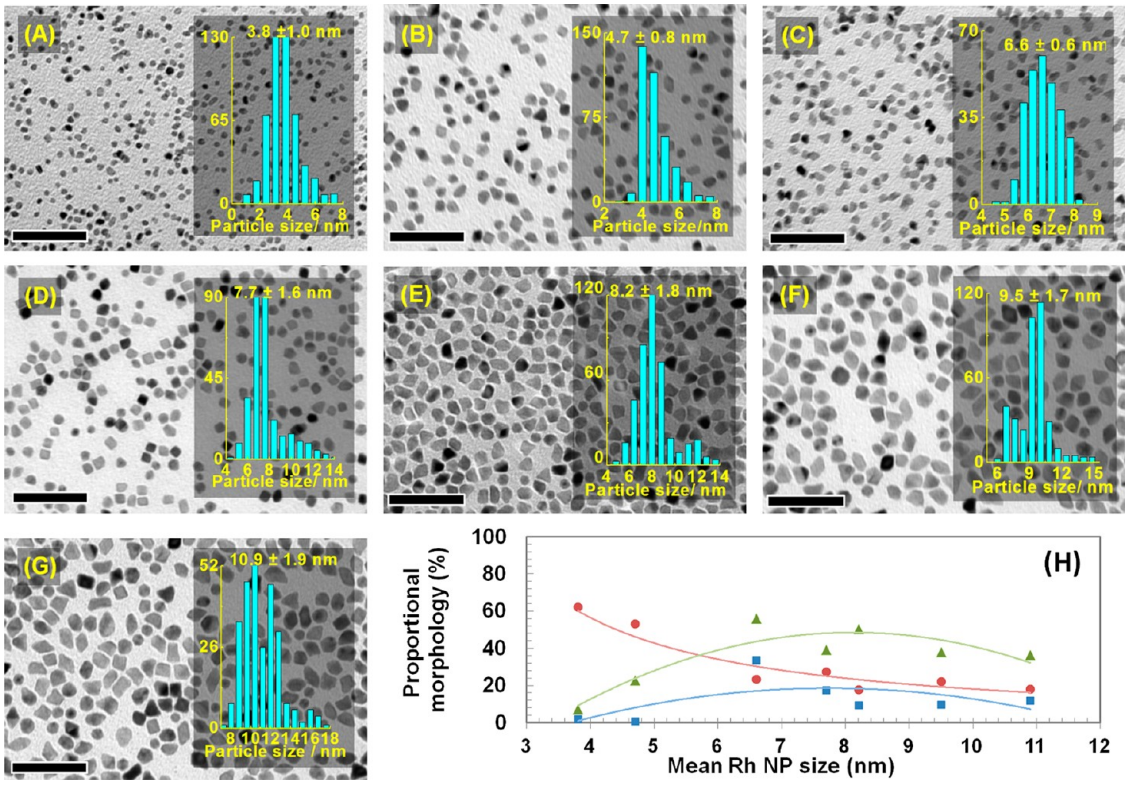

Figure 4. Growth products from conventional heating at 150 °C: (A) 0.1 mmol; (B) 0.2 mmol; (C) 0.3 mmol; (D) 0.4 mmol; (E) 0.5 mmol; (F) 0.6 mmol; (G) 0.7 mmol added $RhCl_3$; (H) comparative proportions of RhNP shapes as a function of size (red = cuboctahedra and all other mutlifaceted polyhedra; blue = cubes; green = tetrahedral particles); scale bars = 50 nm.

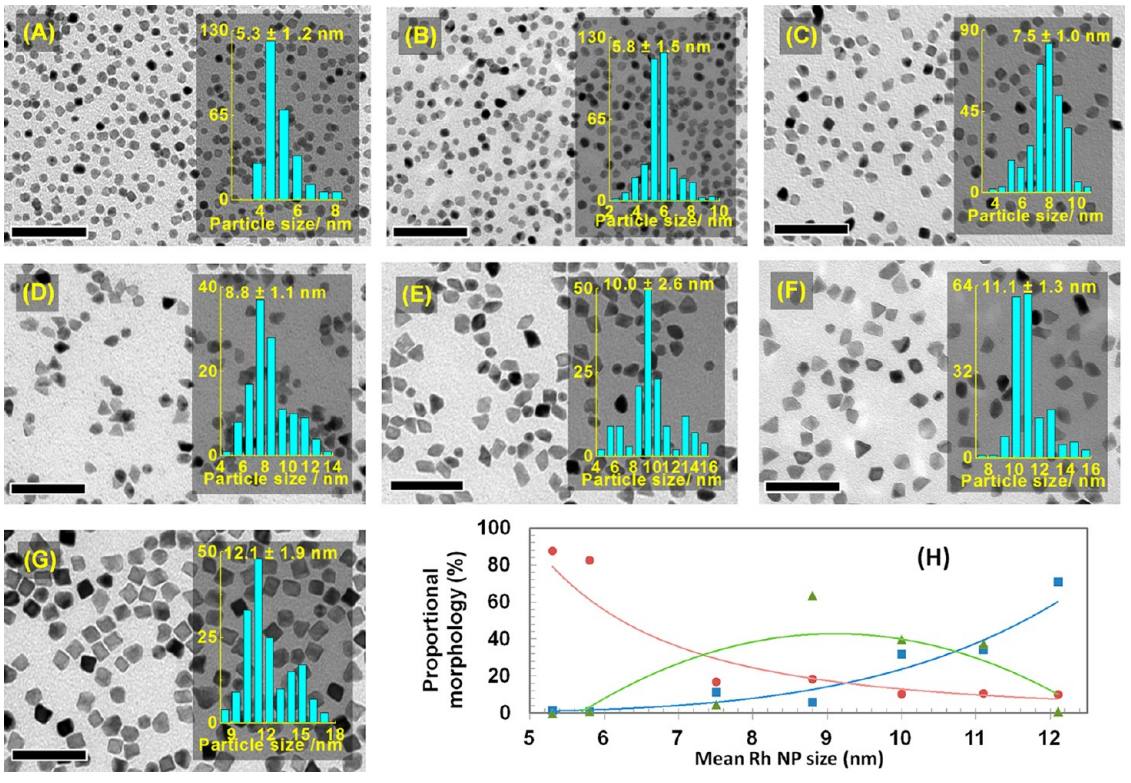

Figure 5. Growth products from microwave-assisted heating at 150 °C: (A) 0.1 mmol; (B) 0.2 mmol; (C) 0.3 mmol; (D) 0.4 mmol; (E) 0.5 mmol; (F) 0.6 mmol; (G) 0.7 mmol added $RhCl_3$; (H) comparative proportions of RhNP shapes as a function of size (red = cuboctahedra and all other mutlifaceted polyhedra; blue = cubes; green = tetrahedral particles); scale bars = 50 nm.

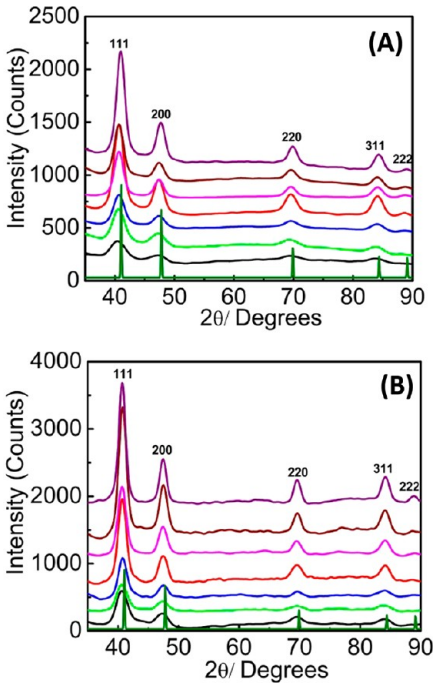

Figure 6. (A) PXRD for CvH-RhNPs, (B) PXRD for MwH-RhNPs: dark green = simulated pattern for fcc Rh; black = RhNP seeds; bottom upward are for overgrown RhNP seeds using the following additional $RhCl_3$: green = 0.1 mmol; blue = 0.2 mmol; red = 0.3 mmol; pink = 0.4 mmol; brown = 0.5 mmol; purple = 0.6 mmol (see Table 1); particle sizes were determined by TEM.

TABLE 1. Intensity Ratios for the 111:200 Integrated Peak Areas[a]

CvH-RhNP (nm)	$I_{(111)/(200)}$	MwH-RhNP (nm)	$I_{(111)/(200)}$
3.8	2.21	4.5	2.37
4.7	2.40	5.8	2.49
6.6	2.72	7.2	2.76
7.7	2.61	8.4	2.97
8.2	2.63	10.0	2.67
9.5	2.82	11.1	2.85
10.9	2.80	12.1	2.45

[a] Particle sizes shown were obtained from TEM images.

addition to weaker reflections corresponding to shorted *d* spacings.[59]

Analogous Microwave Synthesis of Pd and Pt Nanoparticles. In light of the high degree of reproducibility of the synthetic method described above for the synthesis of RhNPs, we attempted to prepare other noble metal nanoparticles by substitution of the metal precursor. Often, procedures are not widely applicable for the preparation of different metal NPs for a number of synthetic reasons. For example, per the synthetic protocol described in this work, precursors such as $HAuCl_4$ do not undergo reduction in ethylene glycol at 150 °C; meanwhile, other common precursors that can be reduced at lower temperatures are unfortunately insoluble in glycols. However, a limited number of readily available precursors can be used in place of $RhCl_3$ without the need to alter any other reaction parameters. K_2MCl_4 (M = Pd(II), Pt(II)) are good examples of compatible precursors that can be employed. Using the RhNP nucleation and growth method, it was possible to prepare MwH-PdNPs and PtNPs with control over size and structure akin to the RhNPs discussed above to yield small cuboctahedra with defined edges (Figure 8A,C). However, by CvH, a range of sizes and morphologies were obtained (Figure 8B,D); the CvH-NPs were mostly poorly formed rice-shaped particles. It is worth noting that the reaction protocol was carefully optimized for the targeted synthesis of RhNPs using $RhCl_3$, so we were pleasantly surprised that Pd(II) and Pt(II) salts gave such promising results under the same conditions. It is very likely that minor alterations to reoptimize the procedure for each specific metal precursor (syringe pump addition profile, total solvent volume, *etc.*) would achieve an even higher degree of synthetic control.

Microwave-Assisted Polymer–Ligand Exchange. In order to further explore the potential advantages of Mw-assisted chemistry with the RhNPs, several ligand exchange reactions were attempted for the *in situ* displacement of PVP with alternative monomeric capping agents. From an entropic standpoint, it is not straightforward to displace high molecular weight capping agents such as PVP. However, for ultimate catalytic applications of the NPs, it is highly desirable to employ more labile capping agents that can be removed under facile conditions.[60–63] In comparison to polymers, molecular stabilizing agents are particularly preferable because they can be removed without the need for high-temperature treatment, which may otherwise cause nanoparticle restructuring and/or carbonization. A series of reactions were pursued in which as-synthesized RhNPs of varying sizes were reacted in the presence of 1:1 mixtures of oleylamine and oleic acid. These form ammonium carboxylate anion/cation pairs that are known to act as effective stabilizing agents *via* the formation of moderately strong ionic interactions at the RhNP surface.[60–63] To our pleasant surprise, the desired ligand exchange was successfully effected under MwH irradiation after 1 h of heating at 150 °C (Figure 9). Importantly, the ligand exchange reaction did not result in any noticeable change to the average particle size or morphology, as demonstrated for 5.8 nm RhNPs (Figure 9A,B). FT-IR spectroscopy of reactants and products after precipitation confirmed the complete displacement of PVP and incorporation of the oleylamine/oleic acid (Figure 9C). The broad C=O stretching band of PVP at *ca.* 1650 cm^{-1} and less intense C–H modes (*ca.* 1288 cm^{-1}) were lost and replaced by strong antisymmetric and symmetric C–O vibrations modes of the carboxylate groups at *ca.* 1555 and 1418 cm^{-1}, respectively, in addition to a new N–H bending mode at 1350 cm^{-1}. Unlike the original PVP-capped RhNPs, the resulting alkyl-capped RhNPs were

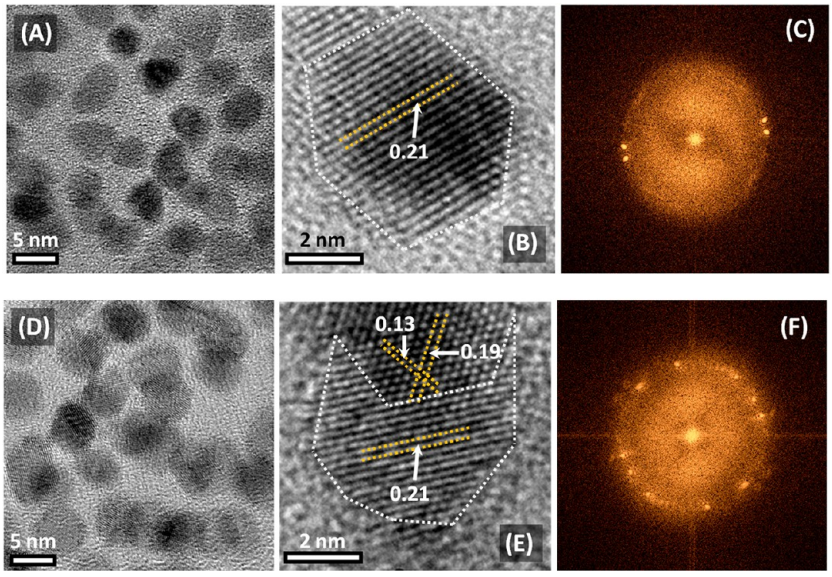

Figure 7. (A) HRTEM of CvH 4.7 nm RhNPs; (B) individual particle exhibiting predominantly {111} surface structure (indexed using Gatan software); (C) corresponding FFT map; (D) HRTEM of 5.8 nm MwH-RhNPs; (E) example of multifaceted surface structure of MwH-RhNPs; (F) corresponding FFT map.

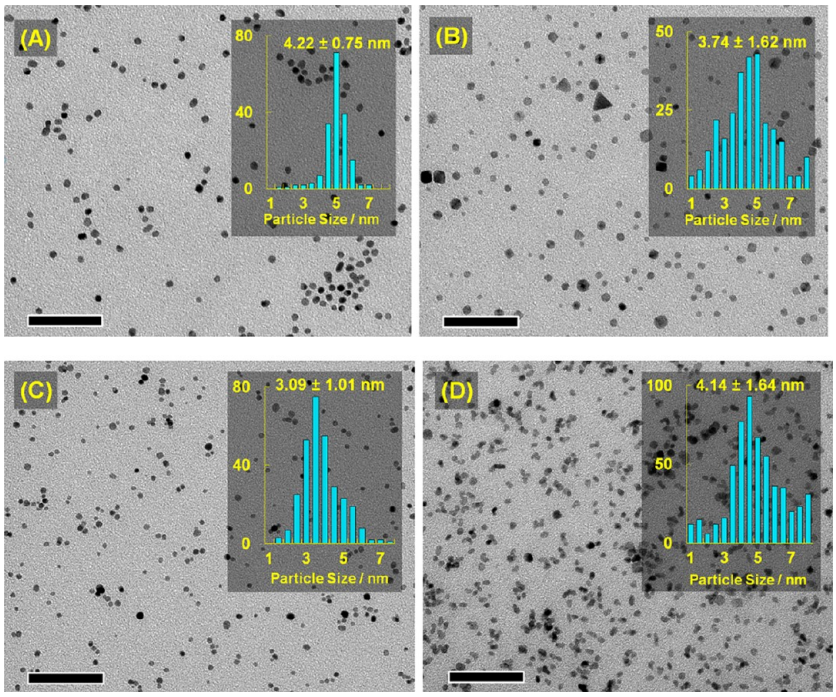

Figure 8. Application of the syringe pump nucleation and growth method to K_2MCl_4 (M = Pd, Pt) precursors: (A) MwH-PdNPs; (B) CvH-PdNPs; (C) MwH-PtNPs; (D) CvH-PtNPs; scale bars = 50 nm.

easily dispersed into solutions of hexanes or toluene to give deep brown suspensions that were stable indefinitely without significant precipitation.

In stark contrast, attempts to perform similar ligand exchange reactions by CvH failed to achieve complete displacement of PVP after 1−2 h of heating at the same temperature employed in the Mw experiment (Figure S10). In all instances, products contained significant PVP and FT-IR showed only very weak bands characteristic of oleylamine or oleic acid. Elemental microanalysis of PVP-capped Rh, Pd, and PtNPs obtained from both CvH and MwH methods indicates that a similar amount of PVP is incorporated in all instances (based on %N and %M values; see Table S1). Therefore, it is reasonable to assume that the observed pronounced benefit of MwH in the ligand exchange process is because PVP is more easily removed from the nanoparticle under Mw irradiation (rather than because less PVP was incorporated into the MwH-RhNPs). It is difficult to directly probe the effect of Mw excitation upon PVP because microwave

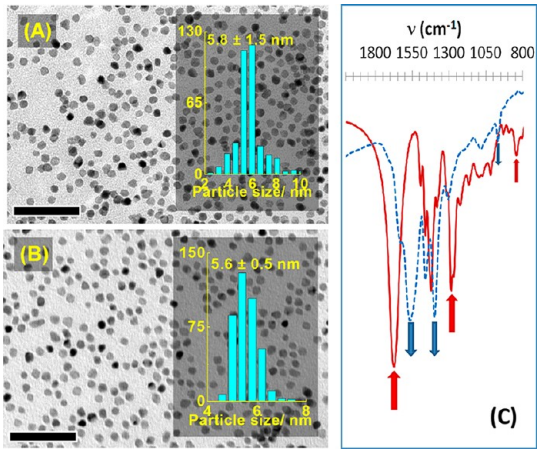

Figure 9. Microwave-assisted ligand exchange study with 5.8 nm RhNPs; (A) original PVP-capped NPs; (B) oleylamine/oleic acid-capped NPs; (C) comparative FT-IR spectra (red = PVP-capped, blue = oleylamine/oleic acid-capped); scale bars = 50 nm.

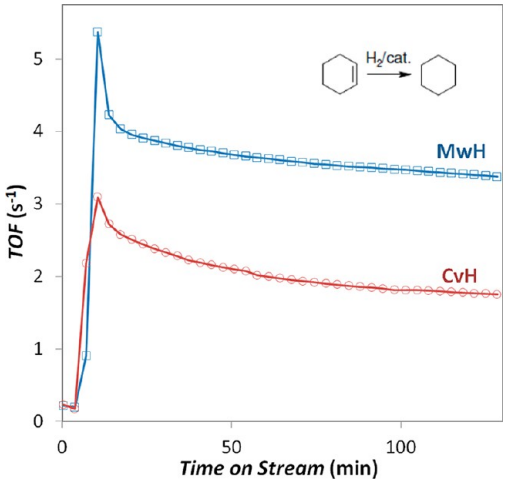

Figure 10. Comparative catalytic performances of the MwH- and CvH-RhNP/SiO_2 materials in the hydrogenation of cyclohexene at 27 °C.

spectroscopy is primarily a gas-phase technique. However, since microwaves are accepted to interact most strongly with the electric charges of polar organic species in solution,[48−51] it is feasible that surface-bound C═O moieties in each PVP monomer are rotationally excited by the Mw field and are thus more easily released from the NP surface. In an attempt to investigate this supposition, we replaced ethylene glycol as the solvent in which the ligand exchange process was carried out with 1-methyl-2-pyrrolidone (*N*-methlypyrrolidone; NMP), which is itself the PVP monomer. Under otherwise identical conditions, it was still possible to completely effect the ligand exchange of PVP with oleylamine/oleic acid under MwH, while CvH was equally unsuccessful (Figure S11). This strongly suggests that the ethylene glycol does not play an intrinsic role in promoting the ligand exchange process. Furthermore, we attempted to synthesize directly RhNPs using oleylamine/oleic acid in place of PVP, *via* the standard MwH syringe pump method. This only gave very poorly defined seeds (Figure S12). It was equally not possible to grow these seeds into larger particles, thus underlining the important role played by PVP in the formation of defined NPs and therefore the subsequent need for means to refunctionalize the preformed NPs with alternative ligands.

Comparative Catalytic Performance of MwH and CvH RhNPs. As stated in the introduction, the catalytic performance of the noble metal NPs is of ultimate interest from an application standpoint. To assess the relative catalytic properties as a function of heating method, cyclohexene hydrogenation was studied, using similarly sized RhNPs obtained from the CvH and MwH methods described herein. Specifically, fresh batches of 12.4 ± 2.1 nm MwH-Rh cubes and 10.1 ± 1.8 nm CvH-RhNPs of mixed morphology (Figure S13A,B) were each directly supported on amorphous silica by simple sonication of suspensions of the as-synthesized PVP-capped RhNPs with acid-washed and precalcined silica. The resulting composites were isolated by filtration. Characterization by TEM confirmed bulk uniformity and attachment of the NPs without agglomeration (Figure S13C,D), and elemental microanalysis was employed to determine percent metal loading (MwH = 1.82; CvH = 2.02%). Milligram quantities of the RhNP/SiO_2 catalyst materials were then studied in the vapor-phase hydrogenation of cyclohexene with H_2 gas, using a single-pass flow reactor with online analysis performed by gas chromatography (GC) sampling of the exit mixture at 3.4 min intervals. Importantly, all reactions were studied at 27 °C without the need for any pretreatment (*e.g.*, high-temperature calcination) to remove the PVP capping agent. Upon exposure to the reactant stream, both catalysts underwent a short initial induction period (*ca.* 4 min) which was followed by a sharp increase in TOF (turnover frequency; units of Rh surface site per second) for the hydrogenation of cyclohexene to cyclohexane (Figure 10). Both CvH and MwH catalysts reached steady state after 20 min. The most striking result from this study was the 2-fold higher steady-state TOF observed for the MwH catalyst (3.40 s^{-1} *versus* 1.77 s^{-1} for the CvH catalyst; Figure 10).[64] The associated activation energies were 5.6 and 8.3 kJ mol^{-1}, respectively (Figure S16). On the basis of these data, the superior hydrogenation ability of the MwH-RhNP catalyst is most likely because there are more accessible Rh surface sites with more highly crystalline/well-defined (100) surfaces in the MwH-synthesized particles. To demonstrate the recyclability of the RhNP-SiO_2 catalysts, further runs were also performed using the same MwH-RhNP/SiO_2 catalyst, which showed no significant decrease in steady-state TOF after 2 h on stream (Figure S14). It is important to note that, because the catalysts were operated at low temperature without any pretreatment, TEM analysis of the postreaction catalysts confirmed that no significant

morphological changes occurred to the individual supported RhNPs (Figure S15).

CONCLUSIONS

A number of beneficial effects of microwave irradiation as an attractive alternative to conventional, convective heating have been demonstrated in the one-pot nucleation and growth of polymer-capped noble metal nanoparticles. Microwave heating was found to have a marked effect on both RhNP nucleation and growth mechanisms, using the popular and convenient wet method of metal halide precursor reduction by hot ethylene glycol in the presence of PVP. Nucleation is fast when performed under microwave heating and also leads to highly uniform particles, unlike identical reactions that were heated conventionally using an oil bath. Nucleation of RhNPs by microwave heating was sufficiently rapid that growth processes quickly become dominant, thus resulting in initial particles that were always significantly larger than their conventionally prepared counterparts. The preparation of very small (<3 nm) NPs was possible under microwave heating by using a short burst of irradiation to induce nucleation of all metal precursor instantaneously. Microwave-assisted RhNP growth was highly reproducible, and the method provided access to both tetrahedral particles of intermediate sizes (5−8 nm) and larger Rh cubes (10+ nm). A very attractive additional capability of microwave-assisted heating was demonstrated for the complete exchange of PVP capping agent with oleylamine and oleic acid and appeared to be intrinsically linked to microwave-based rotational excitation of the polymer. The exchange reaction proceeded quickly and cleanly under microwave irradiation at 150 °C, without any detectable change to the size or morphology of the RhNPs. However, similar ligand exchange was difficult to achieve under conventional heating. The superior catalytic activity of microwave-prepared cubic RhNPs *versus* conventionally prepared RhNPs with assorted morphologies was also demonstrated in the vapor-phase hydrogenation of cyclohexene. In-depth heterogeneous catalysis studies using microwave-synthesized noble metal nanoparticles are presently ongoing.

EXPERIMENTAL SECTION

Materials. Rhodium trichloride hydrate ($RhCl_3 \cdot xH_2O$, 98%; Johnson Matthey), potassium tetrachloropalladate (K_2PdCl_4, 99%; Strem Chemicals), potassium tetrachloroplatinate (K_2PtCl_4; 99.9%; Alfa Aesar), poly(vinylpyrrolidone) (PVP, $\langle M_w \rangle$ = 55 000; Sigma Aldrich), ethylene glycol ($\{CH_2OH\}_2$, 99.8%; Fisher Scientific), *N*-methylpyrrolidone (OmniSolv, 99.86%), and anhydrous cyclohexene (Alfa Aesar, ≥99%) were used as received. Acid-washed silica gel 60 (0.06−0.2 mm, 70-230 mesh; Alfa Aesar) for catalytic studies was employed as received. All gases (Praxair) used in catalytic studies were 99.9995+% purity. All other reagents and solvents (analytical grade) were employed without further purification unless stated otherwise. TEM grids (200 mesh Cu/Formvar; Ted Pella, Inc.) were prepared by drop-casting ethanol solutions of RhNPs that were evaporated to dryness in air.

Methods. A MARS 5 (CEM Corp.) microwave system with a maximum power of 1600 W (2.45 GHz) was used to perform all microwave-based reactions. Throughout the course of the experiment, the reaction temperature was finely controlled by power modulation *via* a RTP-300+ fiber-optic temperature sensor, located in a beaker of solvent identical to that employed in the reaction. *Note: Insertion of the temperature probe directly into the reaction vessel should be avoided; buildup of solid RhNP product on the probe sheath during the course of the reaction may lead to sparking and ignition.* A 50 cm^3 round-bottomed flask with side arm inlet and fitted with water-cooled reflux condenser was placed in the center of the microwave cavity. The solvent and reactants were magnetically stirred (medium speed setting), and Rh precursor was then added directly into the stirred solvent through a disposable, fine-bore Teflon tube that was maintained at a position below the solvent level, to ensure constant addition rate and to prevent droplet formation. The rate of Rh precursor addition was controlled using an Aladdin programmable syringe pump (WPI, Inc.) that was directly attached to the Teflon tubing (see Supporting Information for a full schematic of the apparatus). The reactions were carried out at ambient pressure in air, with venting at the top of the reflux condenser *via* a three-way stopcock. For corresponding reactions conducted under conventional heating, the same apparatus was employed, albeit outside of the microwave cavity. Heating of the solvent was achieved using a simple mineral oil heat bath atop a hot plate/stirrer fitted with a thermocouple temperature-feedback control. The stirring rate was matched to that of the microwave (1100 rpm). Prior to each new reaction, glassware was thoroughly cleaned in a two-stage acid−base wash (12.0 M HCl aq, 1−2 days; 5 M NaOH in *i*-PrOH/H_2O, 1−2 days), followed by oven drying at 110 °C.

Characterization. Transmission electron microscopy (TEM) images were obtained from a FEI Tecnai microscope operating at 80 kV. The samples were prepared by drop-casting a single aliquot of nanoparticles dispersed in ethanol onto 200 mesh copper Formvar grids (Ted Pella Inc.) and allowing for subsequent evaporation in air. Nanoparticle sizes and standard deviations were derived by measuring a minimum of 200 individual particles per experiment and by averaging multiple images from samples obtained from at least two separate syntheses. Individual particles were measured using Image-J (http://rsbweb.nih.gov/ij), which finds the area of each nanoparticle by pixel counting. High-resolution TEM (HRTEM) was performed using a JEOL 2010F transmission electron microscope, operated at 200 keV using a field-emission gun with 0.19 nm point-to-point resolution. Powder X-ray diffraction patterns were recorded with a Bruker AXS D8 diffractometer using a Cu Kα source (1.5418 Å) operated at 40 kV and 40 mA; spectra were collected using a scan speed of 3° min^{-1} with a step width of 0.02° (2θ). FT-IR data were collected using a Cary 5000 UV−vis NIR spectrometer equipped with a double beam and a wavelength range of 175−3300 nm. Elemental microanalysis and ICP-OES were performed by QTI Intertek, NJ.

Synthesis of RhNPs. A solution of poly(vinylpyrrolidone) (200 mg, 1.8 mmol) in ethylene glycol (15.0 cm^3) was prepared directly in the reaction vessel and brought to 150 °C with stirring. A second solution of $RhCl_3 \cdot xH_2O$ (40.0 mg, 0.19 mmol) was prepared in the same solvent (5.0 cm^3) and loaded into a fresh 10 cm^3 disposable syringe. For the nucleation phase of the reaction, 2.5 cm^3 of the precursor solution was injected into the hot stirred PVP solution at a rate of 3.8−45.8 mmol h^{-1} (11.5 mmol h^{-1} in the optimized case). The color of the solution rapidly became brown/black. In order to study the seed products, aliquots were removed within 30 s of completion of the initial precursor injection. The seed mixture was stirred for 30 min at 150 °C, after which the remaining 2.5 cm^3 of precursor was slowly added to promote seeded growth (0.75−22.9 mmol

h^{-1}; 0.75 mmol h^{-1} in the optimized method). The mixture was stirred for an additional 30 min at 150 °C after completion of precursor addition. The reaction was then cooled rapidly by transferring the reactor vessel to an ice–water bath. The RhNPs were precipitated by adding acetone (*ca.* 60 cm^3) to give a black suspension, which was briefly sonicated (1 min). The precipitate was then isolated by ultracentrifugation (5 krpm, 5 min), and the pale yellow supernatant was decanted away to leave a black solid. This was further purified to remove excess PVP and ethylene glycol by 3–4 cycles of dissolution in ethanol (15 cm^3) followed by precipitation with hexane (75 cm^3) and isolation by centrifugation. The final products were redispersed in ethanol and stored at room temperature. Larger RhNPs of desired size were synthesized by controlled addition of 0.2–0.7 mmol $RhCl_3$ in ethylene glycol (5 cm^3) into the preformed Rh NPs seeds, at 0.75 mmol h^{-1} *via* syringe pump.

Synthesis of PdNPs and PtNPs. PVP (135 mg, 1.23 mmol) was dissolved in ethylene glycol (15.0 cm^3) and heated to 150 °C, at which point a second solution of the metal precursor $K_2[PdCl_4]$ (20 mg, 0.061 mmol) in ethylene glycol (5.0 cm^3) was added using the syringe pump procedure as described above. During the seeding phase, 2.5 cm^3 of the Pd^{2+} solution was added to the hot polymer solution at 3.66 mmol h^{-1} to yield a dark brown solution. The solution was stirred for 30 min at 150 °C, and then the remaining 2.5 cm^3 of metal precursor was added at 0.24 mmol h^{-1}. After a further 30 min, the reaction was worked up identically as for the RhNPs. For PtNPs, $K_2[PtCl_4]$ (78 mg, 0.19 mmol) and PVP (422 mg, 3.8 mmol) were employed; 2.5 cm^3 of the metal precursor was added at a rate of 11.4 mmol h^{-1}, and after 30 min, the remainder was added at a rate of 0.76 mmol h^{-1}. All other reaction conditions and methods (temperature, reaction time, and purification) were as stated above.

Ligand Exchange. Five milligrams of dried PVP-capped RhNPs prepared using the above microwave or conventional heating method (11.4/0.76 mmol h^{-1} seeding/growth) was dissolved in ethylene glycol (15 cm^3), to which oleic acid (2.0 cm^3) and oleylamine (2.0 cm^3) were added *via* syringe. The partitioned mixture was heated to 150 °C for 1 h under stirring, using the standard apparatus configuration. After this time, the lower glycol fraction had become almost colorless, while the upper layer was brown/black. After separation, excess ethanol (*ca.* 50 cm^3) was added to the upper layer, causing precipitation, and the solids were isolated by centrifugation (2 krpm, 1 min). The oleic acid/oleylamine-capped RhNPs were further purified by washing with more ethanol (80 cm^3) and using brief bursts of sonication treatment. The final material was readily soluble in hexanes. For the analogous reactions performed in 1-methyl-2-pyrrolidone (NMP) solvent, ethylene glycol was substituted with NMP (17 cm^3), while all other conditions were identical to those described above.

Catalytic Studies. The catalysts were prepared by addition of precalcined SiO_2 (400 mg) to suspensions of 10–12 mg of PVP-capped RhNPs in ethanol/H_2O (1:4). The slurries were sonicated (10 min), isolated by filtration, washed with copious amounts of ethanol/H_2O, and dried at 65 °C. For each catalytic study, a small amount of the composite catalyst (*ca.* 10–20 mg) was loaded into a custom-made quartz U-tube, suspended above a D3-porosity frit. The sample was topped with acid-washed and calcined sand, heated to 27 °C, and then the sample and entire reactor line (quartz, heated to 90 °C) was purged with the reactant gas mixture (H_2/He 1:1) for 45 min. Catalysis commenced with introduction of cyclohexene vapor into the gas stream *via* an in-line saturator fitted with fritted bubbler. All data was obtained in real-time by automated pneumatically gated sampling of the exhaust stream, directly into an HP Agilent 6890 GC fitted with Restek Stabiliwax 15 m column and tandem FID and TCD detectors. Activity values (μmol of product g $catalyst^{-1}$ s^{-1}) were calculated using raw FID area counts that were first normalized using standard correction factors, then converted into the units shown using the raw catalyst mass. Corresponding turnover frequency (TOF) values (metal surface site s^{-1}) were calculated using the metal wt % loading (obtained directly from ICP-OES of the freshly prepared catalyst material) and estimation of the % of exposed surface atoms (calculated using the average NP size obtained from TEM images and assuming cubic NP shapes for MwH samples and cuboctahedral NPs for CvH samples). Activation energies were determined by collection of steady-state activity values at five temperatures (in the range of 27–82 °C; see Figure S16).

Conflict of Interest: The authors declare no competing financial interest.

Acknowledgment. The authors acknowledge Dr. Vince M. Lynch (UT Austin; X-ray), The American Chemical Society Petroleum Research Fund (#51948-DNI3), and The Welch Foundation (F-1738) for funding, and the National Science Foundation for X-ray equipment (Grant No. 0741973).

Supporting Information Available: TEM images for all nucleation studies under both Cv and Mw heating; TEM images for the effect of fast growth by rapid precursor addition; TEM images showing the effect of elevated reaction temperatures; additional HRTEM images for CvH- and MwH-RhNPs; EDX data; TEM and FT-IR data for NMP-based and unsuccessful CvH ligand exchange experiments; additional catalysis data; elemental microanalysis and ICP-OES data. This material is available free of charge *via* the Internet at http://pubs.acs.org.

REFERENCES AND NOTES

1. Barnard, A. S.; Lin, X. M.; Curtiss, L. A. Equilibrium Morphology of Face-Centered Cubic Gold Nanoparticles >3 nm and the Shape Changes Induced by Temperature. *J. Phys. Chem. B* **2005**, *109*, 24465–24472.
2. Cuenya, B. R. Synthesis and Catalytic Properties of Metal Nanoparticles: Size, Shape, Support, Composition, and Oxidation State Effects. *Thin Solid Films* **2010**, *518*, 3127–3150.
3. Shultz, M. D.; Reveles, J. U.; Khanna, S. N.; Carpenter, E. E. Reactive Nature of Dopamine as a Surface Functionalization Agent in Iron Oxide Nanoparticles. *J. Am. Chem. Soc.* **2007**, *129*, 2482–2487.
4. Wu, N. Q.; Wang, J.; Tafen, D.; Wang, H.; Zheng, J. G.; Lewis, J. P.; Liu, X. G.; Leonard, S. S.; Manivannan, A. Shape-Enhanced Photocatalytic Activity of Single-Crystalline Anatase TiO_2(101) Nanobelts. *J. Am. Chem. Soc.* **2010**, *132*, 6679–6685.
5. Hammer, B. Special Sites at Noble and Late Transition Metal Catalysts. *Top. Catal.* **2006**, *37*, 3–16.
6. Somorjai, G. A.; York, R. L.; Butcher, D.; Park, J. Y. The Evolution of Model Catalytic Systems; Studies of Structure, Bonding and Dynamics from Single Crystal Metal Surfaces to Nanoparticles, and from Low Pressure $<10^{-3}$ Torr to High Pressure $>10^{-3}$ Torr to Liquid Interfaces. *Phys. Chem. Chem. Phys.* **2007**, *9*, 3500–3513.
7. Zhou, W. P.; Lewera, A.; Larsen, R.; Masel, R. I.; Bagus, P. S.; Wieckowski, A. Size Effects in Electronic and Catalytic Properties of Unsupported Palladium Nanoparticles in Electro-oxidation of Formic Acid. *J. Phys. Chem. B* **2006**, *110*, 13393–13398.
8. Semagina, N. V.; Bykov, A. V.; Sulman, E. M.; Matveeva, V. G.; Sidorov, S. N.; Dubrovina, L. V.; Valetsky, P. M.; Kiselyova, O. I.; Khokhlov, A. R.; Stein, B.; *et al.* Selective Dehydrolinalool Hydrogenation with Poly(ethylene oxide)-*Block*-Poly-2-vinylpyridine Micelles Filled with Pd Nanoparticles. *J. Mol. Catal. A* **2004**, *208*, 273–284.
9. Thomas, J. M.; Johnson, B. F. G.; Raja, R.; Sankar, G.; Midgley, P. A. High-Performance Nanocatalysts for Single-Step Hydrogenations. *Acc. Chem. Res.* **2003**, *36*, 20–30.
10. Astruc, D.; Lu, F.; Aranzaes, J. R. Nanoparticles as Recyclable Catalysts: The Frontier between Homogeneous and Heterogeneous Catalysis. *Angew. Chem., Int. Ed.* **2005**, *44*, 7852–7872.
11. Shen, L.; Bao, N.; Yanagisawa, K.; Domen, K.; Gupta, A.; Grimes, C. A. Direct Synthesis of ZnO Nanoparticles by a Solution-Free Mechanochemical Reaction. *Nanotechnology* **2006**, *17*, 5117–5123.
12. Wang, J. S.; Yin, S.; Komatsu, M.; Zhang, Q. W.; Saito, F.; Sato, T. Photo-oxidation Properties of Nitrogen Doped $SrTiO_3$ Made by Mechanical Activation. *Appl. Catal. B* **2004**, *52*, 11–21.

13. Bigioni, T. P.; Lin, X. M.; Nguyen, T. T.; Corwin, E. I.; Witten, T. A.; Jaeger, H. M. Kinetically Driven Self Assembly of Highly Ordered Nanoparticle Monolayers. *Nat. Mater.* **2006**, *5*, 265–270.
14. Jana, N. R.; Gearheart, L.; Murphy, C. J. Evidence for Seed-Mediated Nucleation in the Chemical Reduction of Gold Salts to Gold Nanoparticles. *Chem. Mater.* **2001**, *13*, 2313–2322.
15. Sau, T. K.; Murphy, C. J. Room Temperature, High-Yield Synthesis of Multiple Shapes of Gold Nanoparticles in Aqueous Solution. *J. Am. Chem. Soc.* **2004**, *126*, 8648–8649.
16. Sun, Y. G.; Xia, Y. N. Shape-Controlled Synthesis of Gold and Silver Nanoparticles. *Science* **2002**, *298*, 2176–2179.
17. Manna, L.; Scher, E. C.; Alivisatos, A. P. Synthesis of Soluble and Processable Rod, Arrow, Teardrop, and Tetrapod-Shaped CdSe Nanocrystals. *J. Am. Chem. Soc.* **2000**, *122*, 12700–12706.
18. Murphy, C. J.; San, T. K.; Gole, A. M.; Orendorff, C. J.; Gao, J. X.; Gou, L.; Hunyadi, S. E.; Li, T. Anisotropic Metal Nanoparticles: Synthesis, Assembly, and Optical Applications. *J. Phys. Chem. B* **2005**, *109*, 13857–13870.
19. Marqusee, J. A.; Ross, J. Theory of Ostwald Ripening—Competitive Growth and Its Dependence on Volume Fraction. *J. Chem. Phys.* **1984**, *80*, 536–543.
20. Stoeva, S.; Klabunde, K. J.; Sorensen, C. M.; Dragieva, I. Gram-Scale Synthesis of Monodisperse Gold Colloids by the Solvated Metal Atom Dispersion Method and Digestive Ripening and Their Organization into Two- and Three-Dimensional Structures. *J. Am. Chem. Soc.* **2002**, *124*, 2305–2311.
21. Ahmadi, T. S.; Wang, Z. L.; Green, T. C.; Henglein, A.; El-Sayed, M. A. Shape-Controlled Synthesis of Colloidal Platinum Nanoparticles. *Science* **1996**, *272*, 1924–1925.
22. Grace, A. N.; Pandian, K. One Pot Synthesis of Polymer Protected Pt, Pd, Ag and Ru Nanoparticles and Nanoprisms under Reflux and Microwave Mode of Heating in Glycerol—A Comparative Study. *Mater. Chem. Phys.* **2007**, *104*, 191–198.
23. Millstone, J. E.; Hurst, S. J.; Metraux, G. S.; Cutler, J. I.; Mirkin, C. A. Colloidal Gold and Silver Triangular Nanoprisms. *Small* **2009**, *5*, 646–664.
24. Narayanan, R.; El-Sayed, M. A. Effect of Nanocatalysis in Colloidal Solution on the Tetrahedral and Cubic Nanoparticle SHAPE: Electron-Transfer Reaction Catalyzed by Platinum Nanoparticles. *J. Phys. Chem. B* **2004**, *108*, 5726–5733.
25. Wang, Z. L.; Petroski, J. M.; Green, T. C.; El-Sayed, M. A. Shape Transformation and Surface Melting of Cubic and Tetrahedral Platinum Nanocrystals. *J. Phys. Chem. B* **1998**, *102*, 6145–6151.
26. Humphrey, S. M.; Grass, M. E.; Habas, S. E.; Niesz, K.; Somorjai, G. A.; Tilley, T. D. Rhodium Nanoparticles from Cluster Seeds: Control of Size and Shape by Precursor Addition Rate. *Nano Lett.* **2007**, *7*, 785–790.
27. Zettsu, N.; McLellan, J. M.; Wiley, B.; Yin, Y.; Li, Z.-Y.; Xia, Y. Synthesis, Stability, and Surface Plasmonic Properties of Rhodium Multipods, and Their Use as Substrates for Surface-Enhanced Raman Scattering. *Angew. Chem., Int. Ed.* **2006**, *45*, 1288–1292.
28. Cushing, B. L.; Kolesnichenko, V. L.; O'Connor, C. J. Recent Advances in the Liquid-Phase Syntheses of Inorganic Nanoparticles. *Chem. Rev.* **2004**, *104*, 3893–3946.
29. Ashida, T.; Miura, K.; Nomoto, T.; Yagi, S.; Sumida, H.; Kutluk, G.; Soda, K.; Namatame, H.; Taniguchi, M. Synthesis and Characterization of Rh(PVP) Nanoparticles Studied by XPS and NEXAFS. *Surf. Sci.* **2007**, *601*, 3898–3901.
30. Biacchi, A. J.; Schaak, R. E. The Solvent Matters: Kinetic *versus* Thermodynamic Shape Control in the Polyol Synthesis of Rhodium Nanoparticles. *ACS Nano* **2011**, *5*, 8089–8099.
31. Durap, F.; Zahmakiran, M.; Ozkar, S. Water Soluble Laurate-Stabilized Rhodium(0) Nanoclusters Catalyst with Unprecedented Catalytic Lifetime in the Hydrolytic Dehydrogenation of Ammonia-Borane. *Appl. Catal. A* **2009**, *369*, 53–59.
32. Ewers, T. D.; Sra, A. K.; Norris, B. C.; Cable, R. E.; Cheng, C. H.; Shantz, D. F.; Schaak, R. E. Spontaneous Hierarchical Assembly of Rhodium Nanoparticles into Spherical Aggregates and Superlattices. *Chem. Mater.* **2005**, *17*, 514–520.
33. Filot, I. A. W.; Shetty, S. G.; Hensen, E. J. M.; van Santen, R. A. Size and Topological Effects of Rhodium Surfaces, Clusters and Nanoparticles on the Dissociation of CO. *J. Phys. Chem. C* **2011**, *115*, 14204–14212.
34. Harada, M.; Abe, D.; Kimura, Y. Synthesis of Colloidal Dispersions of Rhodium Nanoparticles under High Temperatures and High Pressures. *J. Colloid Interface Sci.* **2005**, *292*, 113–121.
35. Hoefelmeyer, J. D.; Liu, H.; Somorjai, G. A.; Tilley, T. D. Reverse Micelle Synthesis of Rhodium Nanoparticles. *J. Colloid Interface Sci.* **2007**, *309*, 86–93.
36. Hoefelmeyer, J. D.; Niesz, K.; Somorjai, G. A.; Tilley, T. D. Radial Anisotropic Growth of Rhodium Nanoparticles. *Nano Lett.* **2005**, *5*, 435–438.
37. Jang, K.; Kim, H. J.; Son, S. U. Low-Temperature Synthesis of Ultrathin Rhodium Nanoplates *via* Molecular Orbital Symmetry Interaction between Rhodium Precursors. *Chem. Mater.* **2010**, *22*, 1273–1275.
38. Leger, B.; Denicourt-Nowicki, A.; Olivier-Bourbigou, H.; Roucoux, A. Rhodium Nanocatalysts Stabilized by Various Bipyridine Ligands in Nonaqueous Ionic Liquids: Influence of the Bipyridine Coordination Modes in Arene Catalytic Hydrogenation. *Inorg. Chem.* **2008**, *47*, 9090–9096.
39. Mittendorfer, F.; Seriani, N.; Dubay, O.; Kresse, G. Morphology of Mesoscopic Rh and Pd Nanoparticles under Oxidizing Conditions. *Phys. Rev. B* **2007**, *76*, 233413.
40. Mu, X. D.; Meng, J. Q.; Li, Z. C.; Kou, Y. Rhodium Nanoparticles Stabilized by Ionic Copolymers in Ionic Liquids: Long Lifetime Nanocluster Catalysts for Benzene Hydrogenation. *J. Am. Chem. Soc.* **2005**, *127*, 9694–9695.
41. Ojeda, M.; Rojas, S.; Boutonnet, M.; Perez-Alonso, F. J.; Garcia-Garcia, F. J.; Fierro, J. L. G. Synthesis of Rh Nanoparticles by the Microemulsion Technology—Particle Size Effect on the $CO+H_2$ Reaction. *Appl. Catal. A* **2004**, *274*, 33–41.
42. Pradhan, M.; Sarkar, S.; Sinha, A. K.; Basu, M.; Pal, T. High-Yield Synthesis of 1D Rh Nanostructures from Surfactant Mediated Reductive Pathway and Their Shape Transformation. *J. Phys. Chem. C* **2011**, *114*, 16129–16142.
43. Quek, X. Y.; Guan, Y. J.; van Santen, R. A.; Hensen, E. J. M. Ionic-Liquid-Stabilized Rhodium Nanoparticles for Citral Cyclodehydration. *ChemSusChem* **2010**, *3*, 1264–1267.
44. Redel, E.; Kramer, J.; Thomann, R.; Janiak, C. Synthesis of Co, Rh and Ir Nanoparticles from Metal Carbonyls in Ionic Liquids and Their Use as Biphasic Liquid-Liquid Hydrogenation Nanocatalysts for Cyclohexene. *J. Organomet. Chem.* **2009**, *694*, 1069–1075.
45. Zhang, H.; Li, W. Y.; Jin, M. S.; Zeng, J. E.; Yu, T. K.; Yang, D. R.; Xia, Y. N. Controlling the Morphology of Rhodium Nanocrystals by Manipulating the Growth Kinetics with a Syringe Pump. *Nano Lett.* **2011**, *11*, 898–903.
46. Zhang, Y. W.; Grass, M. E.; Kuhn, J. N.; Tao, F.; Habas, S. E.; Huang, W. Y.; Yang, P. D.; Somorjai, G. A. Highly Selective Synthesis of Cataytically Active Monodisperse Rhodium Nanocubes. *J. Am. Chem. Soc.* **2008**, *130*, 5868–5869.
47. Zhang, Y. W.; Grass, M. E.; Huang, W. Y.; Somorjai, G. A. Seedless Polyol Synthesis and CO Oxidation Activity of Monodisperse (111) and (100) Oriented Rhodium Nanocrystals in Sub-10 nm Sizes. *Langmuir* **2011**, *26*, 16463–16468.
48. Kappe, C. O. Controlled Microwave Heating in Modern Organic Synthesis. *Angew. Chem., Int. Ed.* **2004**, *43*, 6250–6284.
49. Lidstrom, P.; Tierney, J.; Wathey, B.; Westman, J. Microwave Assisted Organic Synthesis—A Review. *Tetrahedron* **2001**, *57*, 9225–9283.
50. Bilecka, I.; Niederberger, M. Microwave Chemistry for Inorganic Nanomaterials Synthesis. *Nanoscale* **2010**, *2*, 1358–1374.
51. Nadagouda, M. N.; Speth, T. F.; Varma, R. S. Microwave-Assisted Green Synthesis of Silver Nanostructures. *Acc. Chem. Res.* **2011**, *44*, 469–478.

52. Panda, A. B.; Glaspell, G.; El-Shall, M. S. Microwave Synthesis of Highly Aligned Ultra Narrow Semiconductor Rods and Wires. *J. Am. Chem. Soc.* **2006**, *128*, 2790–2791.
53. Zedan, A. F.; Sappal, S.; Moussa, S.; El-Shall, M. S. Ligand-Controlled Microwave Synthesis of Cubic and Hexagonal CdSe Nanocrystals Supported on Graphene. Photoluminescene Quenching by Graphene. *J. Phys. Chem. C* **2010**, *114*, 19920–19927.
54. Panda, A. B.; Glaspell, G.; El-Shall, M. S. Microwave Synthesis and Optical Properties of Uniform Nanorods and Nanoplates of Rare Earth Oxides. *J. Phys. Chem. C* **2007**, *111*, 1861–1864.
55. Abdelsayed, V.; Aljarash, A.; El-Shall, M. S. Microwave Synthesis of Bimetallic Nanoalloys and CO Oxidation on Ceria-Supported Nanoalloys. *Chem. Mater.* **2009**, *21*, 2825–2834.
56. Njoki, P. N.; Wu, W.; Zhao, H.; Hutter, L.; Schiff, E. A.; Maye, M. M. Layer-by-Layer Processing and Optical Properties of Core/Alloy Nanostructures. *J. Am. Chem. Soc.* **2011**, *133*, 5224–5227.
57. Herring, N. P.; AbouZeid, K.; Mohammed, M. B.; Pinsk, J.; El-Shall, M. S. Formation Mechanisms of Gold-Zinc Oxide Hexagonal Nanopyramids by Heterogeneous Nucleation Using Microwave Synthesis. *Langmuir* **2011**, *27*, 15146–15154.
58. Zhang, Y. W.; Grass, M. E.; Habas, S. E.; Tao, F.; Zhang, T. F.; Yang, P. D.; Somorjai, G. A. One-Step Polyol Synthesis and Langmuir−Blodgett Monolayer Formation of Size-Tunable Monodisperse Rhodium Nanocrystals with Catalytically Active (111) Surface Structures. *J. Phys. Chem. C* **2007**, *111*, 12243–12253.
59. Jose-Yacaman, M.; Marin-Almazo, M.; Ascencio, J. A. High Resolution TEM Studies on Palladium Nanoparticles. *J. Mol. Catal. A* **2001**, *173*, 61–74.
60. Borodko, Y.; Humphrey, S. M.; Tilley, T. D.; Frei, H.; Somorjai, G. A. Charge-Transfer Interaction of Poly(vinylpyrrolidone) with Platinum and Rhodium Nanoparticles. *J. Phys. Chem. C* **2007**, *111*, 6288–6295.
61. Bagaria, H. G.; Ada, E. T.; Shamsuzzoha, M.; Nikles, D. E.; Johnson, D. T. Understanding Mercapto Ligand Exchange on the Surface of FePt Nanoparticles. *Langmuir* **2006**, *22*, 7732–7737.
62. Grass, M. E.; Joo, S. H.; Zhang, Y. W.; Somorjai, G. A. Colloidally Synthesized Monodisperse Rh Nanoparticles Supported on SBA-15 for Size- and Pretreatment-Dependent Studies of CO Oxidation. *J. Phys Chem. C* **2009**, *113*, 8616–8623.
63. Borodko, Y.; Habas, S. E.; Koebel, M.; Yang, P.; Frei, H.; Somorjai, G. A. Probing the Interaction of Poly(vinylpyrrolidone) with Platinum Nanocrystals by UV-Raman and FTIR. *J. Phys. Chem. B* **2006**, *110*, 23052–23059.
64. Cimpeanu, V.; Kočevar, M.; Parvulescu, V. I.; Leitner, W. Preparation of Rhodium Nanoparticles in Carbon Dioxide Induced Ionic Liquids and Their Application to Selective Hydrogenation. *Angew. Chem., Int. Ed.* **2008**, *48*, 1085–1088.